Palli, Samu-Ville; Hiltunen, Paavo; Kosonen, Milla; Tamminen, Aleksi; Ala-Laurinaho, Juha; Taylor, Zachary

Submillimeter-wave holograms and imaging neural network : Experiments at 220-330 GHz

Submillimeter-wave holograms and imaging neural network: experiments at 220-330 GHz

Samu-Ville Pälli, Paavo Hiltunen, Milla Kosonen, Aleksi Tamminen, Juha Ala-Laurinaho, et al.

Submillimeter-wave holograms and imaging neural network: Experiments at 220-330 GHz

Samu-Ville Pälli, Paavo Hiltunen, Milla Kosonen, Aleksi Tamminen,
Juha Ala-Laurinaho, and Zachary Taylor
Aalto University Department of Electronics and Nanoengineering, MilliLab
Maarintie 8, Espoo, 02150, Finland

ABSTRACT

We present the experimental results of a submillimeter-wave standoff imaging system based on a frequency-diverse hologram and image reconstruction via machine learning at 220-330 GHz. The imaging system operates in a single-pixel, monostatic configuration consisting of a transceiver together with a frequency-diverse phase hologram to interrogate the region of interest with quasirandom field patterns. The spatial reflectivity distribution in the region of interest is embedded in the wide-band frequency spectrum of the back-reflected signal and the images are acquired without mechanical or electrical scanning. Images from a visible-light camera are used as the ground truth of the target elements. The targets are scanned in the region of interest, while the wide-band reflection spectrum for the target is measured. The collected image-signal pair data are used to train a deconvolutional neural network for image reconstruction with the submillimeter-wave reflection spectra as input. In experiments, a corner-cube reflector and a complex test target made of copper foam were imaged in a 28-degree field of view at a distance of 600 mm from the imaging system. The effect of bandwidth on image quality is evaluated using 10-40 GHz bandwidths centered at 275 GHz to image the copper foam target. The resolution in the image predictions was estimated from fitted point-spread functions to be from 12 mm to 30 mm, with the highest resolution at the broadest bandwidth. We have correlated the measured field patterns at the region of interest with the mean squared error (MSE) of the predicted corner-cube images to analyze the effect of field characteristics on imaging accuracy. The results demonstrate increased accuracy in locations with high electric field amplitude and variation over the imaging bandwidth.

Keywords: Hologram, imaging, neural network, submillimeter-wave

1. INTRODUCTION

The unique properties of submillimeter waves provide an effective approach to various imaging and sensing applications. Many of these applications, such as medical imaging and personnel screening, require real-time imagery of the target. Submillimeter-wave real-time imaging systems are commonly based on scanning the beam in the region of interest (RoI) electronically or mechanically [1],[2]. Electronic scanning methods apply an array of amplitude- or phase-shifting elements to manipulate the beam shape and direction. In mechanical scanning, the focal point is steered over the region of interest by mirrors actuated by mechanical drives. Both technologies suffer from complexity of the system hardware. Electrically scanning arrays can have thousands of phase-coherent elements, leading to increasing costs especially at shorter wavelengths. Mechanical systems require routine maintenance and can have a large footprint.

Recently, computational imaging methods have shown promise in simplifying imaging architecture by shifting the complexity to software and image reconstruction algorithms [3]. With computational imaging methods, spatially and temporally quasi-random illumination is used to interrogate the RoI. The reflectivity information from the target is encoded in the backscattered signal, allowing image reconstruction without pixel-by-pixel scanning over the RoI. Frequency-diverse imaging is a computational imaging technique relying on frequency-swept sources and engineered frequency-dependent apertures to achieve quasi-random illumination. Strong frequency diversity of the aperture allows imaging with a minimal number of transceivers. The single-pixel camera is an imaging technique where a single sensor or transceiver is multiplexed to different modes using masks or coded apertures [4],[5]. These coded apertures are used to introduce spatio-temporal modulation to the illuminating field. Various computational imaging systems based on coded apertures have been demonstrated in the literature. Dynamic metasurfaces with active beam control have been used at microwave frequencies [6],[7]. These methods eliminate the need for phase-shifting circuits but still require circuitry to control the aperture. At

millimeter-waves, frequency-diverse imaging has been demonstrated using over-moded cavity resonators and metamaterial apertures [8],[9]. Alternatively, frequency-diverse millimeter-wave imaging using a transceiver array for a 5G base station was presented in [10]. However, these methods are rather complex and require an accurate alignment and characterization of the propagation path to allow image reconstruction. Earlier, we have demonstrated localization with a frequency-diverse hologram together with a terahertz time-domain spectrometer (THz-TDS) operating at 0.1-2.0 THz. [11].

We present the experimental results of a submillimeter-wave standoff imaging system based on a frequency-diverse hologram and image reconstruction via machine learning at 220-330 GHz. The imaging system utilizes a single transceiver together with a frequency-diverse hologram to interrogate the RoI without mechanical or electrical scanning. Experiments with the imaging system were carried out using copper-foam targets at the region of interest. A trained neural network was used to reconstruct the image of the target from the measured back-reflected submillimeter-wave signal.

2. IMAGING SYSTEM

The proposed imaging system is based on illuminating the region of interest through a dispersive transmission-type hologram. The hologram element is designed to disperse the incident field with maximum transverse spatial variation at the RoI over a wide frequency band while maintaining good diffraction efficiency. This allows illumination of the RoI with high amplitude and spatial variation. A single transceiver is used to measure the back-reflected spectrum from the RoI through the hologram. Each frequency point of the back-reflected signal consists of a reflectivity map of the RoI weighted with the complex spatial field distribution. As the illuminating frequency is swept over a wide bandwidth, the measured wide-band reflection spectrum contains numerous, uniquely weighted representations of the RoI. The key hypothesis of the presented method is that the wide-band reflection spectrum from the region of interest is able to convey enough information to reconstruct an image of the target. A trained deep neural network is used to reconstruct the image with the reflection spectrum as an input. Figure 1 shows a sketch of the imaging system.
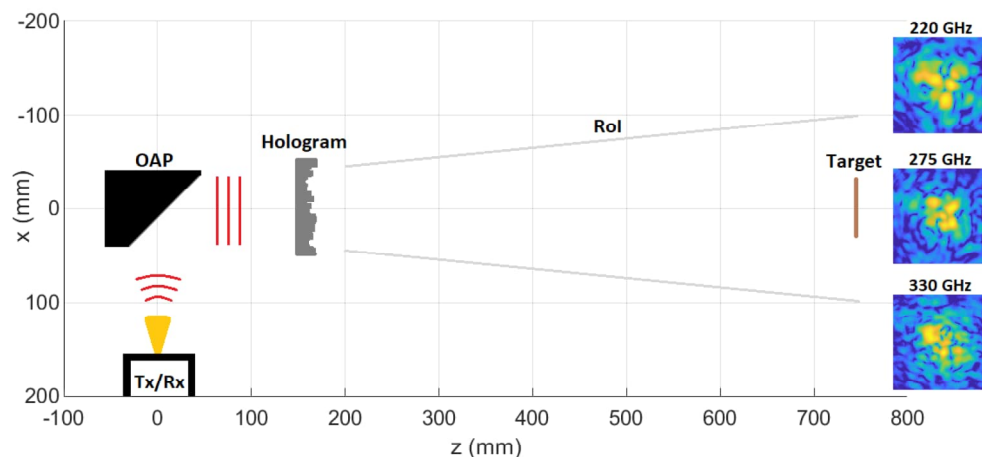

Figure 1. Schematic representation of the imaging method. A Gaussian beam from the transceiver is collimated by an off-axis parabolic mirror (OAP). The hologram modulates the phase of the collimated field to create spatially varying, frequency-diverse field distributions at the region of interest. The back-reflected signal contains the reflectivity map of the RoI, sampled with different spatial field distribution at each frequency point.

2.1 Frequency-diverse hologram

The dispersive, frequency-diverse phase hologram is manufactured on a 30-mm thick block of low-loss cross-linked polystyrene (Rexolite 1422) with relative dielectric permittivity of $\varepsilon_r = 2.52 - j0.0005$ [12]. The aperture size of the hologram is 76.2×76.2 mm^2. The hologram has a CNC-machined quasirandom surface relief, designed to modulate the phase of the incident field creating complex, frequency-diverse field patterns at the region of interest. The design process of the hologram surface relief and experimental results of the dispersive beam pattern in the RoI are presented in detail in [13]. The surface relief has five distinct height levels with a step height of 5.1 mm, corresponding to 5.9-8.9 wavelengths from 220 to 330 GHz.

2.2 Imaging setup

The imaging setup consists of a vector network analyzer (N2552A PNA by Keysight Technologies, Inc.) coupled to a submillimeter-wave extension WR3.4-VNAX (Virginia Diodes Inc.) to achieve the imaging frequency band of 220-330 GHz. A Pickett-Potter dual-mode horn antenna (Radiometer Physics GbmH) coupled to the submillimeter-wave extension served as a Gaussian feed for a 90-degree off-axis parabolic mirror (Edmund Optics) collimating the beam. The OAP mirror has a diameter of 76.2 mm and an effective focal length of 127 mm, corresponding to the distance between the feed horn and mirror focus. The hologram modulates the collimated field and produces frequency-diverse field patterns at the region of interest, 600 mm from the hologram.

In the imaging experiments, the target in the RoI was the Aalto University logo, made of 5-mm thick, porous copper foam with a pore size of 1-2 mm. As the pore size is comparable to the imaging wavelength, the copper foam acts as a diffuse scatterer. The width and height of the logo were 132 mm and 100 mm, respectively, with the smallest detail size of ~6 mm The logo was secured to the radar-absorbing material and mounted on a planar near-field scanner (NSI-200 V-5x5 by Near-Field Systems Inc.) in the region of interest. The imaging system was built on an optical table and aligned with the target copper-foam target in RoI. The imaging setup and copper-foam material are illustrated in Figure 2. In addition to the copper-foam targets, a 12.7-mm corner cube reflector is used in evaluating the spatial distribution of the image quality. The corner-cube reflector can be co-located with the open-ended waveguide antenna probe for comparing the measured dispersive field with the image quality.
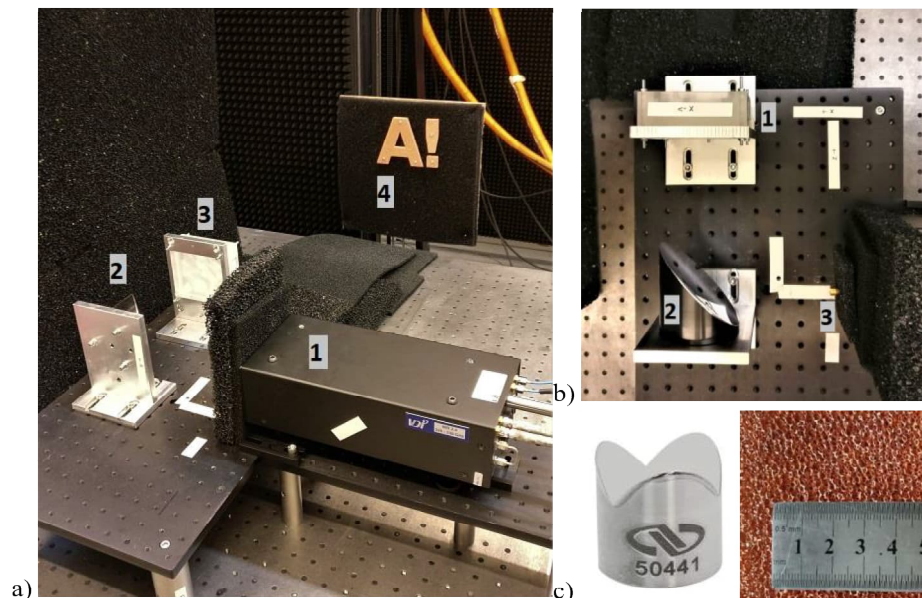

Figure 2. (a) The overview of the imaging setup: 1) Submillimeter-wave transceiver, 2) OAP mirror, 3) hologram, and 4) copper-foam target. (b) Close-up of the quasi-optics: 1) Hologram, 2) OAP mirror, and 3) Pickett-Potter horn. c) Close-up photographs of the corner-cube reflector and copper foam.

3. NEURAL NETWORK AND IMAGING RESULTS

A deconvolutional neural network is trained to images of the targets in the RoI. The training data is the reflection spectrum from the RoI with the targets in different locations. The labels in neural network training are visible-light images of the targets in their corresponding locations in the RoI. The neural network is based on a fully-connected part, which shapes the spectral content to layer with dimensions after which the neural network uses deconvolutional layers to expand the data into images. Figure 3 shows the topology of the neural network. The processed reflection spectrum from the RoI is given as a 2002-element long vector with real and imaginary parts in the input layer of the network. The neural networks progress with a fully-connected layer, dropout layer (p = 50 %), and reshape layer to data with dimensions of 1000 × 2 × 2. In the standard notation of neural networks, the dimensions with 1000 elements are considered channels, and the dimensions with 2 elements are related to spatial domains in each channel. From there onwards, the network consists of 2-dimensional deconvolutional layers with each output layer dimension of $o' = s(i' - 1) + k$, where $s = 2$ is stride, i is input layer dimension, and $k = 3$ is kernel size [14], [15]. As a result of the selected parameters, the dimension of the layer outputs is

increased to 256×256 across seven deconvolutional layers. At the same time, the number of channels is reduced monotonously from 1000 (input to deconvolution) to 1 (final image). The activation function between the layers is rectified linear unit and sigmoid function at the output. The neural network work is carried out in Keras machine learning API [15]. Adam optimizer is used with the categorical cross-entropy as the loss function. The training is carried out at a learning rate of $\alpha = 0.001$ and the training is let run 500 epochs for both datasets.
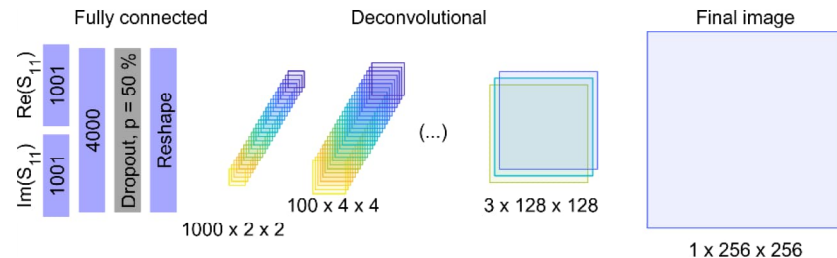

Figure 3. Topology of the neural network for imaging the Aalto logos. The input layer consists of the concatenated real and imaginary parts of the reflection spectrum. A dropout layer is used to reduce overfitting and increase the network robustness to input data. Seven deconvolutional layers expand the spectral data into images.

3.1 Training data

To gather training data for the imaging neural network, the copper foam test targets and the corner-cube reflector were translated in the region of interest in 200-mm $\times$ 200-mm area. The back-reflected signal (S_{11} parameter) from the targets was measured in 10201 different locations, corresponding to 101×101 raster scan. The raster scan of the target is done only for the acquisition of the training data, and it is not required in the actual imaging process. A trained neural network is able to reconstruct the image from a single, static S_{11} measurement. The measured S_{11} is time-gated, normalized, and concatenated to an array including the real and imaginary parts of the S_{11}. Examples of the processed training data and the corresponding images are shown in Figure 4.
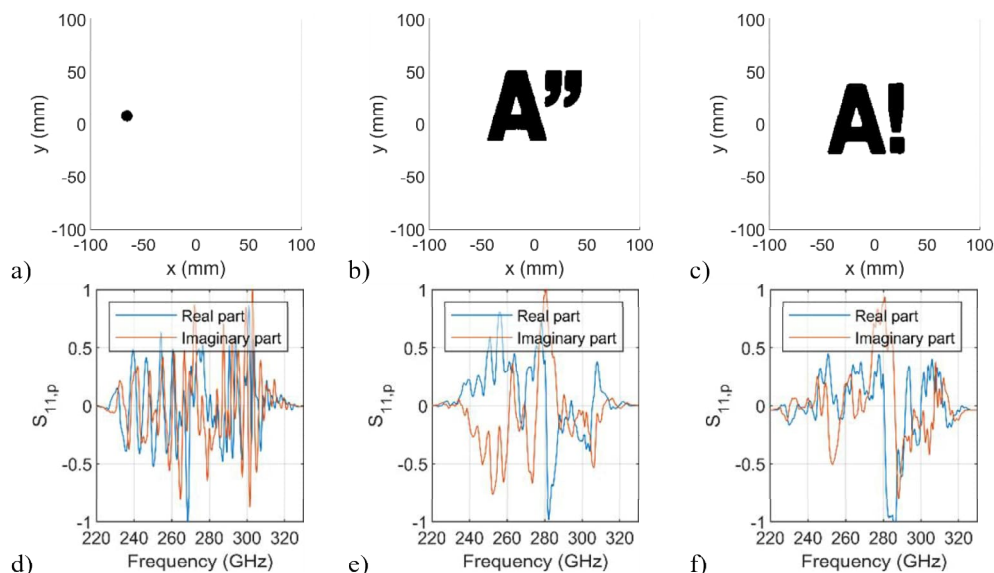

Figure 4. Images of the targets: a) Circular aperture of the corner cube and b, c) Aalto University logos. The corresponding processed S_{11} for each case is in d-f).

3.2 Imaging results

Imaging results are evaluated with the corner-cube reflector and with the Aalto logos. For the corner-cube images, the full bandwidth of 220-330 GHz is utilized and for the Aalto logos, narrower bandwidths of 10-40 GHz centered at 275 GHz are used. The images of the corner cube in different locations of the RoI are compared with the separately measured radiation pattern in the RoI, which allows for evaluating the image quality against the characteristics of the spatially varying dispersive field. The images of the corner-cube reflector are assumed as 12.7-mm disks in the RoI. The images of the Aalto University logos are evaluated as realistic examples of more complex targets being imaged. Also, the limited bandwidth

allows for evaluating the performance in typical cases of, e.g., integrated FMCW radars, instead of the state-of-art vector network analyzer with bandwidth covering the full waveguide band. Examples of predicted images with the corner-cube target and Aalto logos are shown in Figure 5. For the corner cube, ten example images are summed into a single figure for convenience.

The image quality is evaluated as the mean squared error in pixel values for the corner cubes, defined as

$$MSE = \frac{1}{N_{px}} \sum_i |\text{prediction}_i - \text{label}_i|,$$ (1)

where prediction_i is the ith pixel brightness in the predicted image and label_i is the ith pixel brightness in the label image. The dispersive field in the RoI has been measured with an open-ended waveguide as a near-field probe connected to the VNA extender with the probe aperture centered with the corner-cube aperture.
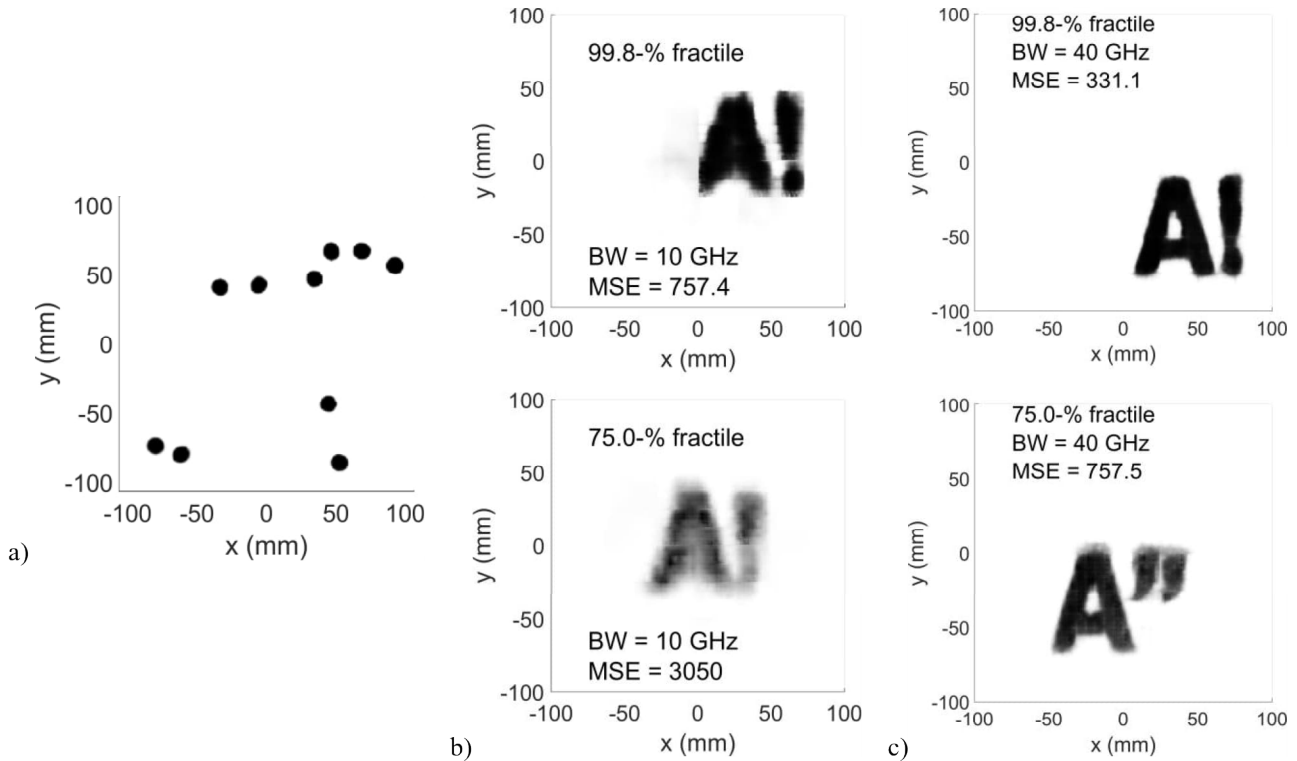

Figure 5. Predicted images with a) corner-cube target and Aalto logos in bandwidths of b) 10 GHz and c) 40 GHz. The Aalto logo predictions are shown in fractile of 99.8 % and 75 % when sorted in ascending MSE.

Figures 6 a and b show the radiation patterns in the RoI at 220 GHz and 330 GHz overlayed with markers showing the location of the corner-cube centroid. Marker size represents the MSE. The MSE is small in areas where the amplitude of the field is significant, while close to the field minima, the error increases. However, no strong correlation between the characteristics of the field in RoI and image quality has been found. Figures 6 c and d show the standard deviation and mean of the field amplitude in RoI with the MSE overlaid, which in general suggest successful image prediction close in areas with large variation in the field as well as relative high amplitude.
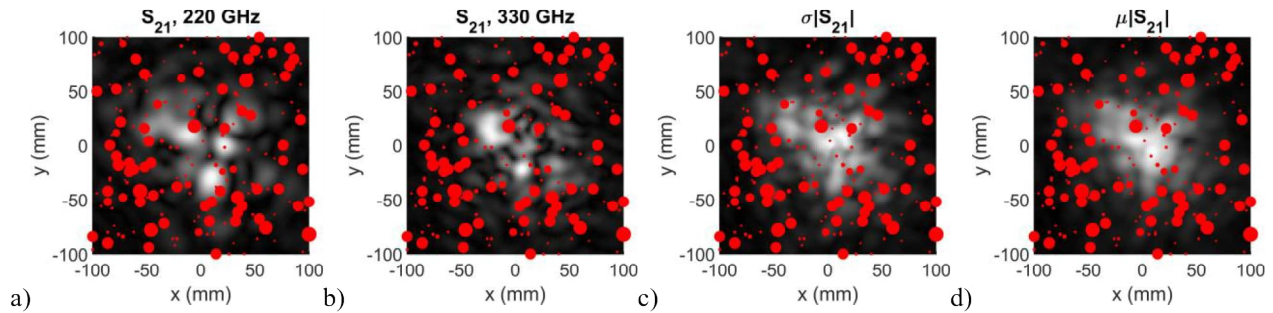
Figure 6. Radiation patterns at a) 220 GHz and b) 330 GHz as well as c) standard deviation and d) average of the measured S_{21} across the 220-330 GHz bandwidth. The markers show the corner cube location, and the size of the markers shows the value of the MSE.

3.3 Estimates of PSF

The point-spread function in the predicted images is estimated through a fitting method, where the image labels are convoluted with a Gaussian kernel. The convolution introduces spatial blur to the images, which models the finite resolution in the predicted images. The Gaussian σ-value is varied to minimize the sum of squares of the difference between the predicted image and blurred image label [16]. The estimated full-width at half maximum (FWHM) of the PSF in the predicted images at bandwidths of 10-40 GHz centered at 275 GHz is shown in Figure 7. With the 10-GHz bandwidth, the FWHM is mostly between 20 mm and 40 mm with significant variation. At 20-, 30-, and 40-GHz bandwidths, the average FWHM reduces to 20 mm, 15 mm, and 12 mm. Also, the variation of FWHM decreases inversely to the bandwidth from the narrow 10-GHz band to the broad 40-GHz band: 14 mm, 6.6 mm, 4.9 mm, and 3.7 mm.
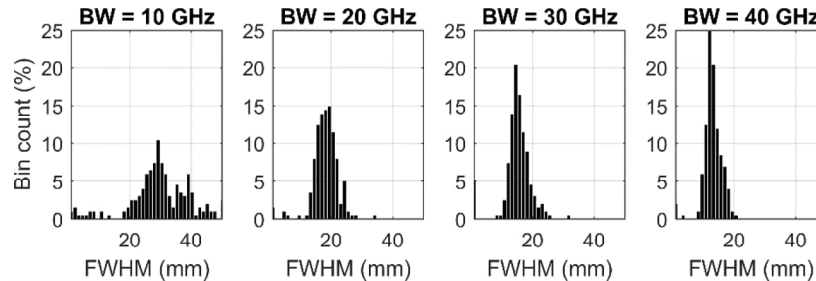

Figure 7. The estimated histogram of the FWHM of the PSF in the predictions of Aalto logo images with different bandwidths.

4. CONCLUSIONS

We have presented experimental results of a submillimeter-wave imaging system based on a frequency-diverse hologram and image reconstruction via machine learning at 220-330 GHz. The imaging system consists of a single static transceiver together with a dispersive, frequency-diverse hologram, producing quasirandom field patterns at the region of interest. The measured wide-band, back-reflected signal contains the spatial reflectivity distribution weighted with complex dispersed field patterns. We have trained a deep neural network to map the reflection spectrum from a corner-cube reflector and a more complex copper foam target into 2D images. We have studied the effect of limited bandwidth on image quality using reflection spectra from bands of 10, 20, 30, and 40 GHz centered at 275 GHz to image the copper foam target. The image predicting neural networks were trained to each band separately and they indicate an increase in image resolution until the 30-GHz band with some improvement at broader bandwidth. As such, the method is suitable for use with a typical integrated MMIC transceiver with about 10-% fractional bandwidth. In addition, we have correlated the measured field patterns at the region of interest with the mean squared error of the predicted corner-cube images to evaluate the effect of field characteristics on imaging accuracy. The results suggest increased prediction accuracy in locations with high field amplitude and variation. The presented imaging system allows efficient computational submillimeter-wave imaging using a single transceiver without mechanical or electrical scanning. The current imaging system is restricted in imaging distance and field of view by the hologram aperture size. We believe that the presented technology can be scaled-up to meet the demands of various imaging applications.

ACKNOWLEDGMENTS

REFERENCES

[1] S. S. Ahmed, A. Schiessl, and L.-P. Schmidt, "A Novel Fully Electronic Active Real-Time Imager Based on a Planar Multistatic Sparse Array," *IEEE Trans. Microw. Theory Techn.,* vol. 59, no. 12, pp. 3567-3576, 2011.

[2] K. B. Cooper, R. J. Dengler, N. Llombart, B. Thomas, G. Chattopadhyay, and P. H. Siegel, "THz Imaging Radar for Standoff Personnel Screening," *IEEE Trans. THz Sci. Technol.,* vol. 1, no. 1, pp. 169-182, 2011.

[3] O. Yurduseven *et al.*, "From microwaves to submillimeter waves: modern advances in computational imaging, radar, and future trends," *Proc. SPIE 10917, Terahertz, RF, Millimeter, and Submillimeter-Wave Technology and Applications XII,* Mar. 2019, Art no. 1091710.

[4] M. F. Duarte *et al.*, "Single-pixel imaging via compressive sampling," *IEEE Signal Process. Mag.,* vol. 25, no. 2, pp. 83-91, 2008.

[5] R. I. Stantchev, X. Yu, T. Blu, and E. Pickwell-MacPherson, "Real-time terahertz imaging with a single-pixel detector," *Nat. Commun.,* vol. 11, no. 1, pp. 1-8, 2020.

[6] T. Sleasman, M. F. Imani, J. N. Gollub, and D. R. Smith, "Dynamic metamaterial aperture for microwave imaging," *Appl. Phys. Lett.,* vol. 107, no. 20, 2015.

[7] O. Yurduseven, D. L. Marks, T. Fromenteze, and D. R. Smith, "Dynamically reconfigurable holographic metasurface aperture for a Mills-Cross monochromatic microwave camera," *Opt Express,* vol. 26, no. 5, pp. 5281-5291, 2018.

[8] T. Fromenteze *et al.*, "Computational imaging using a mode-mixing cavity at microwave frequencies," *Appl. Phys. Lett.,* vol. 106, no. 19, 2015.

[9] T. Zvolensky, V. R. Gowda, J. Gollub, D. L. Marks, and D. R. Smith, "W-Band Sparse Imaging System Using Frequency Diverse Cavity-Fed Metasurface Antennas," *IEEE Access,* vol. 6, pp. 73659-73668, 2018.

[10] M. K. Leino, J. Bergman, J. Ala-Laurinaho, and V. Viikari, "Millimeter-wave frequency-diverse imaging with phased array intended for communications," *Prog. Electromagn. Res. M,* vol. 101, pp. 69-78, 2021.

[11] A. Tamminen, S.-V. Pälli, J. Ala-Laurinaho, A. Aspelin, A. Oinaanoja, and Z. Taylor, "Holograms with neural-network backend for submillimeter-wave beamforming applications," *Proc. SPIE 11411, Passive and Active Millimeter-Wave Imaging XXIII,* Apr. 2020, Art no. 114110C.

[12] J. W. Lamb, "Miscellaneous data on materials for millimetre and submillimetre optics," *J. Infrared Millim. Waves,* vol. 17, no. 12, pp. 1997-2034, 1996.

[13] S.-V. Pälli, A. Tamminen, J. Ala-Laurinaho, and Z. D. Taylor, "Design and Characterization of Phase Holograms for Standoff Localization at Millimeter and Submillimeter Waves," *IEEE Trans. Microw. Theory Techn.,* vol. 70, no. 1, pp. 907-918, 2022.

[14] V. Dumoulin and F. Visin, "A guide to convolution arithmetic for deep learning," *arXiv Preprint,* 2016, Art no. arXiv:1063.07285.

[15] *Keras: the Python deep learning API.* [Online]. Available: https://keras.io/

[16] N. Joshi, R. Szeliski, and D. J. Kriegman, "PSF estimation using sharp edge prediction," in *2008 IEEE Conference on Computer Vision and Pattern Recognition*, 2008, pp. 1-8.